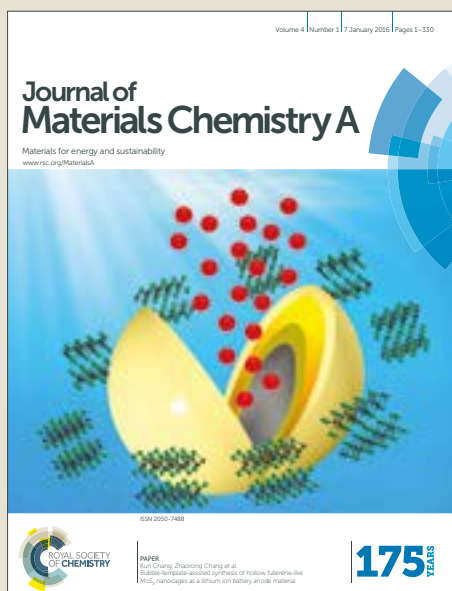


# Journal of Materials Chemistry A

Accepted Manuscript



This article can be cited before page numbers have been issued, to do this please use: Y. Bai, L. Wei, M. Yang, H. Chen, S. Holdren, C. Yao, R. Sun, Y. Pan and D. Liu, *J. Mater. Chem. A*, 2018, DOI: 10.1039/C8TA01242C.



This is an Accepted Manuscript, which has been through the Royal Society of Chemistry peer review process and has been accepted for publication.

Accepted Manuscripts are published online shortly after acceptance, before technical editing, formatting and proof reading. Using this free service, authors can make their results available to the community, in citable form, before we publish the edited article. We will replace this Accepted Manuscript with the edited and formatted Advance Article as soon as it is available.

You can find more information about Accepted Manuscripts in the [author guidelines](#).

Please note that technical editing may introduce minor changes to the text and/or graphics, which may alter content. The journal's standard [Terms & Conditions](#) and the ethical guidelines, outlined in our [author and reviewer resource centre](#), still apply. In no event shall the Royal Society of Chemistry be held responsible for any errors or omissions in this Accepted Manuscript or any consequences arising from the use of any information it contains.

1 **Three-step cascade over one single catalyst: synthesis of 5-(ethoxymethyl)furfural from**  
2 **glucose over hierarchical lamellar multi-functional zeolite catalyst**

3  
4 Yuanyuan Bai<sup>a,b,c</sup>, Wei Lu<sup>a</sup>, Mengfei Yang<sup>d</sup>, Huiyong Chen<sup>d</sup>, Scott Holdren<sup>e</sup>, Chunli Yao<sup>c</sup>,  
5 Runcang Sun<sup>c</sup>, Yanbo Pan<sup>f</sup> and Dongxia Liu<sup>\*a</sup>

6  
7 *<sup>a</sup>Department of Chemical and Biomolecular Engineering, University of Maryland, College Park,*  
8 *MD, 20742, USA*

9 *<sup>b</sup>National Engineering Lab for Pulp and Paper, China National Pulp and Paper Research*  
10 *Institute Co. Ltd., Beijing, 100102, China*

11 *<sup>c</sup>Beijing Key Laboratory of Lignocellulosic Chemistry, Beijing Forestry University, Beijing,*  
12 *100083, China*

13 *<sup>d</sup>School of Chemical Engineering, Northwest University, Xi'an, Shaanxi, 710069, China*

14 *<sup>e</sup> Department of Chemistry and Biochemistry, University of Maryland, College Park, MD, 20742,*  
15 *USA*

16 *<sup>f</sup>Department of Chemical and Biomolecular Engineering, University of Akron, Akron 44325,*  
17 *USA*

18  
19 \*Corresponding author:  
20 Prof. Dongxia Liu  
21 Email: liud@umd.edu  
22 Phone: (+1) 301-405-3522  
23 Fax: (+1) 301-405-0523  
24

25

26

27

28 **Abstract:** The synthesis of hierarchical lamellar zeolites with controlled meso-/microporous  
29 morphology and acidity is an expanding area of research interest for a wide range of  
30 applications. Here, we report a one-step synthesis of hierarchical meso-/microporous lamellar  
31 MFI-Sn/Al zeolite (*i.e.*, containing both Lewis acidic Sn- and Al-sites and Brønsted acidic Al-  
32 O(H)-Si site and its catalytic application for conversion of glucose into 5-(ethoxymethyl)furfural  
33 (EMF). Particularly, the MFI-Sn/Al zeolite was prepared under the assistance of a diquatery  
34 ammonium ( $[\text{C}_{22}\text{H}_{45}\text{-N}^+(\text{CH}_3)_2\text{-C}_6\text{H}_{12}\text{-N}^+(\text{CH}_3)_2\text{-C}_6\text{H}_{13}]\text{Br}^{2-}$ , C<sub>22-6-6</sub>) template in a composition of  
35  $100\text{SiO}_2/5\text{C}_{22-6-6}/18.5\text{Na}_2\text{O}/x\text{Al}_2\text{O}_3/y\text{SnO}_2/2957\text{H}_2\text{O}$  ( $x=0.5, 1, \text{ and } 2, y=1 \text{ and } 2, \text{ respectively}$ ).  
36 The MFI-Sn/Al zeolites innovatively feature dual meso-/microporosity and dual Lewis and  
37 Brønsted acidity, which enabled three-step reaction cascade for EMF synthesis from glucose in  
38 the ethanol solvent. The reaction proceeded via the isomerization of glucose to fructose over  
39 Lewis acidic Sn-sites and dehydration of fructose to 5-hydroxymethylfurfural (HMF) and then  
40 etherification of HMF and ethanol to EMF over the Brønsted acidic Al-O(H)-Si sites. The co-  
41 existence of multiple acidities in one single zeolite catalyst enabled one-pot cascade reactions for  
42 carbohydrate upgrading. The dual meso-/microporosity in the MFI-Sn/Al zeolites facilitated  
43 mass transport in processing of bulky biomass molecules. The balance of both types of acidity  
44 and meso-/microporosity realized EMF yield as high as 44% from the glucose reactant.

45

46 **Keywords:** 5-Ethoxymethylfurfural; Glucose; Biomass; Zeolites; Meso-/microporosity;  
47 Hierarchical structure.

48

49

50

51 **Introduction**

52 Over the past century, the world society has been heavily relied on fossil resources, such as coal,  
53 gas, and oil, to produce human beings' daily needed fuels and chemicals.<sup>1-3</sup> The carbon dioxide  
54 produced from usage of these non-renewable fossil resources has been significantly changing the  
55 climate on earth,<sup>2</sup> and the heavy reliance on these fossil resources makes them more expensive  
56 and less abundant. As a widely available and sustainable carbon source, biomass has the  
57 potential to replace the non-renewable fossil resources for the production of fuels and  
58 chemicals.<sup>4</sup> Lignocellulosic biomass, consisting of 60~80% carbohydrate component,<sup>5</sup> is the  
59 most promising renewable carbon source for production of both fuels and platform chemicals.  
60 Many strategies have been explored for the conversion of carbohydrates in lignocellulosic  
61 biomass into chemicals and fuels.<sup>6-8</sup> The use of an appropriate catalyst plays a crucial role in  
62 achieving high conversion and high selectivity to the end fuel and/or chemical alternative  
63 products in a green and economic process.<sup>9,10</sup>

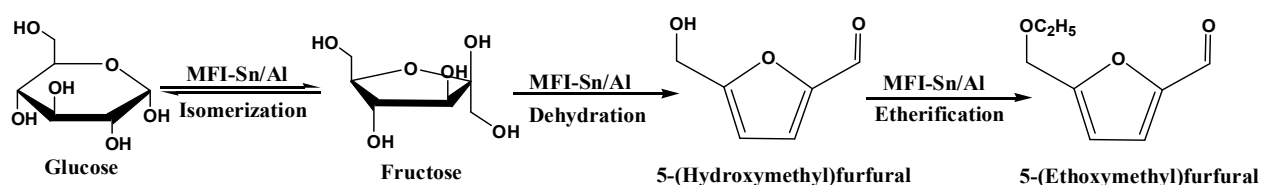
64 5-(Ethoxymethyl)furfural (EMF), a liquid with boiling point of 508 K and an energy density  
65 of 30.3 MJ L<sup>-1</sup>, close to that of diesel (33.6 MJ L<sup>-1</sup>), gasoline (31.1 MJ L<sup>-1</sup>) and ethanol (23.5  
66 MJ L<sup>-1</sup>), is an attractive and potential end biofuel alternative product.<sup>11-13</sup> The synthesis of EMF  
67 from biomass feedstock has been practiced via a single step etherification of 5-  
68 hydroxymethylfurfural (HMF),<sup>14</sup> two-step cascade of dehydration-etherification of fructose,<sup>15</sup>  
69 three-step cascade of decomposition-dehydration-etherification of disaccharide (e.g., sucrose)<sup>16</sup>  
70 or oligosaccharide (e.g., inulin)<sup>17</sup>, and three-step cascade of isomerization-dehydration-  
71 etherification of monosaccharide such as glucose<sup>12</sup> in ethanol solvent. The single-step synthesis  
72 of EMF from HMF can occur over a variety of acidic catalysts<sup>5</sup> with > 90% yield. The high cost

73 and non-stability of HMF, however, restrict its wide application in EMF production. The two-  
74 step and three-step cascade reactions of fructose-based feedstocks on acidic catalysts overcome  
75 the shortcomings in EMF synthesis via the single-step approach, but these saccharides are less  
76 abundant in nature. In contrast, glucose or glucose-based oligosaccharide and polysaccharide is  
77 the most abundant carbohydrate in lignocellulosic biomass.

78 The synthesis of EMF from glucose feedstock is desired, but requires multiple types of  
79 catalysts for different steps in the reaction cascade. For example, a combination of Sn-BEA and  
80 Amberlyst-15 catalysts has been used for glucose conversion to EMF<sup>12</sup>, in which the former  
81 catalyst acts as Lewis acid for isomerization of glucose to fructose and the latter one catalyzes  
82 the dehydration and etherification of fructose to EMF. In this three-step reaction cascade,  
83 transport of reaction intermediates from one catalyst to the other in the reactor is needed, which  
84 might impede the efficiency in EMF production from the process point of view. The usage of  
85 multiple catalysts also complicates the catalyst preparation and/or separation steps if the catalyst  
86 recycling is needed. Multifunctional catalyst, *i.e.*, a single catalyst comprised of structurally  
87 and/or compositionally different active components within nanoscale distance, can enable  
88 multiple reaction steps successively and efficiently in the catalysis cascade. The precise position  
89 of active centers in the multifunctional catalysts, like the enzymatic catalyst systems in nature,<sup>18-</sup>  
90 <sup>20</sup> can also facilitate cooperative catalysis. The synthesis of EMF from glucose or glucose-based  
91 abundant carbohydrates is desired to take place over such a multifunctional catalyst, but such a  
92 catalyst system has been rarely reported.

93 In the present study, we report a hierarchical lamellar multifunctional MFI-Sn/Al zeolite  
94 catalyst that contains dual meso-/microporosity and dual Lewis and Brønsted acidity for glucose  
95 conversion into the EMF product. The MFI-Sn/Al catalyst was prepared via a single-step

96 hydrothermal crystallization method under the assistance of a diquatery ammonium template  
 97 ( $[\text{C}_{22}\text{H}_{45}\text{-N}^+(\text{CH}_3)_2\text{-C}_6\text{H}_{12}\text{-N}^+(\text{CH}_3)_2\text{-C}_6\text{H}_{13}] \text{Br}^{2-}$ ,  $\text{C}_{22-6-6}$ ) in a composition of  $100\text{SiO}_2/5\text{C}_{22-6-6}$   
 98  $/18.5\text{Na}_2\text{O}/x\text{Al}_2\text{O}_3/y\text{SnO}_2/2957\text{H}_2\text{O}$  ( $x=0.5, 1, \text{ and } 2, y=1 \text{ and } 2$ , respectively). The co-existence  
 99 of Sn and Al elements in the MFI-Sn/Al zeolite endows both Lewis acidic Sn- and Al-sites and  
 100 Brønsted acidic Al–O(H)–Si sites for the three-step reaction cascade of isomerization-  
 101 dehydration-etherification in the EMF production (Scheme 1). Tetravalent Sn site has showed  
 102 good performance for catalyzing the isomerization of a series of pentose and hexose sugars with  
 103 activities comparable to biological processes<sup>19,20</sup> by a mechanism similar to enzymatic  
 104 catalysts.<sup>18</sup> Therefore, the Sn-sites in the MFI-Sn/Al catalyst were used to catalyze the  
 105 isomerization step in the reaction cascade. The Brønsted acidic Al–O(H)–Si sites catalyze the  
 106 subsequent dehydration of fructose to HMF and etherification of HMF to EMF product. The  
 107 presence of hierarchical meso- and microporosity in the MFI-Sn/Al catalyst allows for facile  
 108 transport of bulky molecules, and thereby further improving the catalyst performance in this  
 109 reaction cascade. A high EMF yield (44%) has been achieved from glucose conversion over the  
 110 multifunctional MFI-Sn/Al catalyst.



112 **Scheme 1** Schematic illustration of EMF synthesis from glucose via a three-step reaction  
 113 cascade over single MFI-Sn/Al zeolite catalyst.

## 114 Experimental

### 115 Materials

116 Aluminum isopropoxide ( $\text{Al}[\text{OCH}(\text{CH}_3)_2]_3$ , 99.99+% purity), tetraethyl orthosilicate (TEOS,  
117 98%), tetrapropylammonium hydroxide (TPAOH, 40 wt%), D (+)-glucose (98%), D-fructose  
118 (98%), sucrose (98%) and inulin (98%) were purchased from Alfa Aesar. Tin chloride  
119 pentahydrate ( $\text{SnCl}_4 \cdot 5\text{H}_2\text{O}$ , 98%), sodium hydroxide ( $\text{NaOH}$ ,  $\geq 97.0\%$ ), and ammonium nitrate  
120 ( $\text{NH}_4\text{NO}_3$ ,  $\geq 99.0\%$ ) were supplied by Sigma-Aldrich. Deionized (DI) water was used throughout  
121 the experiment. Diquaternary ammonium template ( $[\text{C}_{22}\text{H}_{45}\text{-N}^+(\text{CH}_3)_2\text{-C}_6\text{H}_{12}\text{-N}^+(\text{CH}_3)_2\text{-}$   
122  $\text{C}_6\text{H}_{13}]\text{Br}_2$ , ( $\text{C}_{22-6-6}$ )) was synthesized following the method reported by Choi et al<sup>21</sup> and the  
123 detailed synthesis procedure has been described in our previous work.<sup>22,23</sup>

### 124 **Catalyst preparation**

125 The MFI-Sn/Al zeolite catalysts were synthesized in a one-step hydrothermal crystallization  
126 process using the following recipe:  $100\text{SiO}_2/5\text{C}_{22-6-6}/18.5\text{Na}_2\text{O}/x\text{Al}_2\text{O}_3/y\text{SnO}_2/2957\text{H}_2\text{O}$ , where  
127  $x=0.5, 1$ , and  $2$ ,  $y=1$  and  $2$ , respectively. Typically, the synthesis started by dissolving 0.41 g  
128  $\text{NaOH}$  in 11.50 g DI water, followed by addition of desired amount of  $\text{SnCl}_4 \cdot 5\text{H}_2\text{O}$  and  
129  $\text{Al}[\text{OCH}(\text{CH}_3)_2]_3$ , separately. After a clear solution was formed, 5.78 g TEOS was added and the  
130 resultant mixture was stirred vigorously at room temperature for 8 h. A  $\text{C}_{22-6-6}$  solution was  
131 prepared by dissolving 0.95 g  $\text{C}_{22-6-6}$  in 2.83 g of DI water at 333 K and then added into above  
132 mixture. The resultant zeolite synthesis gel was continuously stirred at room temperature for 2 h.  
133 Finally, the synthesis gel was transferred into a Teflon vessel in a stainless steel autoclave. The  
134 autoclave was tumbled vertically at 30 rpm and 423 K in an oven for 14 days. After the  
135 hydrothermal synthesis, the zeolite products were collected by centrifugation at 6000 rpm for 15  
136 min and then washed by dispersing in DI water. The water washing and centrifugation steps were  
137 repeated 6 times. A vacuum oven was utilized to dry the wet zeolite product at room temperature  
138 overnight. Finally, the zeolite samples were calcined in a flowing air ( $1.67 \text{ mL s}^{-1}$ , ultrapure air,

139 Airgas) at 873 K for 6 h. The obtained samples were named as MFI-Sn/Al (Si/Sn molar ratio,  
140 Si/Al molar ratio). According to the synthesis recipe, the following samples, MFI-Sn/Al  
141 (100/100), MFI-Sn/Al (100/50), MFI-Sn/Al (100/25), MFI-Sn/Al (50/50), MFI-Sn/Al ( $\infty$ /100),  
142 have been prepared, respectively.

143 For comparison purpose, the conventional microporous MFI zeolite containing both Sn and  
144 Al (designated as C-MFI-Sn/Al (100/100)) was prepared according to the work of Mal et al.,<sup>24</sup>  
145 and the synthesis procedure was as follows. Firstly, 0.26 g of SnCl<sub>4</sub>·5H<sub>2</sub>O and 0.15 g of  
146 Al[OCH(CH<sub>3</sub>)<sub>2</sub>]<sub>3</sub> were dissolved with 19.00 g of DI water in a polyethylene bottle. Then, 15.61 g  
147 TEOS was added and the resultant mixture was stirred magnetically for 30 min. 16.50 g TPAOH  
148 solution was then added and the mixture was continuously stirred for 1 h. The molar ratio of the  
149 C-MFI-Sn/Al (100/100) synthesis gel was 100SiO<sub>2</sub>/SnO<sub>2</sub>/0.5Al<sub>2</sub>O<sub>3</sub>/44TPAOH/3430H<sub>2</sub>O. Finally,  
150 the mixture was transferred into a Teflon-lined autoclave and kept at 433 K for 2 days under  
151 static condition. After the synthesis, the sample was collected by centrifugation, washed by DI  
152 water and calcined using the procedures described for preparation of MFI-Sn/Al zeolites above.

153 Prior to catalysis tests, all the zeolite samples were ion-exchanged three times using 1.0 M  
154 aqueous NH<sub>4</sub>NO<sub>3</sub> solution (weight ratio of zeolite to NH<sub>4</sub>NO<sub>3</sub> solution = 1:10) for 3 hours at 353  
155 K. The sample was collected by centrifugation, washed with DI water, and dried at 353 K for 12  
156 h. All zeolite samples in their NH<sub>4</sub><sup>+</sup>-form were treated in air (1.67 mL s<sup>-1</sup>, ultrapure air, Airgas)  
157 by increasing the temperature from ambient to 823 K at 0.167 K s<sup>-1</sup> rate and holding them at this  
158 temperature for 4 h.

### 159 **Catalyst characterization**

160 The scanning electron microscopy (SEM) images taken from a Hitachi Su-70 electron  
161 microscope were used to detect the morphologies of the synthesized zeolite samples. The powder

162 X-ray diffraction (XRD) patterns were recorded using a Bruker D8 Advance Lynx Powder  
163 Diffractometer (LynxEye PSD detector, sealed tube, Cu K $\alpha$  radiation with Ni  $\beta$ -filter) in the  $2\theta$   
164 ranging from  $1.2^\circ$  to  $40^\circ$ . The N<sub>2</sub> adsorption-desorption isotherms were measured at 77 K with  
165 an Autosorb-iQ analyzer (Quantachrome Instruments) to characterize the textual properties of  
166 the zeolite samples. Prior to the measurement, all the zeolite samples were evacuated overnight  
167 at 623 K and 1 mm Hg pressure. The solid state magic angle spinning NMR (MAS NMR) spectra  
168 were recorded at a field of 7 T (Bruker DSX 300) for <sup>29</sup>Si and <sup>27</sup>Al. <sup>29</sup>Si MAS NMR spectra were  
169 recorded at 59.64 MHz using 4 mm rotors at a spinning speed of 10 kHz, a dwell time of 20  $\mu$ s, a  
170  $\pi/2$  pulse of 5.0  $\mu$ s, and a recycle delay of 60 s. The spectra were referenced with respect to 3-  
171 (trimethylsilyl)-1-propanesulfonic acid salt. <sup>27</sup>Al MAS NMR spectra were recorded at 78.22  
172 MHz using 4 mm rotors at 10 kHz spinning speed, a dwell time of 1.0  $\mu$ s, a selective  $\pi/10$  pulse  
173 of 0.6  $\mu$ s, and a recycle delay of 4 s. An aqueous solution of aluminum nitrate (0.1 M) was used  
174 as the reference. The ultraviolet-visible diffuse reflectance spectroscopy (UV-Vis-DRS) was  
175 performed using a Perkin-Elmer Lambda 650S model to understand the structure of the Sn-sites  
176 in zeolite samples. The integrating sphere is 60 mm and is made by LabSphere. The coating in  
177 the LabSphere 60 mm integrating attachment is Spectrolong. Typical scan rate was 1 nm/second  
178 and the scan range was from 200 nm to 800 nm. All the spectra were recorded in ambient  
179 condition.

### 180 **Composition and acidity measurement**

181 The Si, Al, and Sn contents of zeolite samples were determined by inductively coupled plasma  
182 atomic emission spectroscopy (ICP-AES, iCAP 6500 dual view). The concentration of active  
183 Brønsted acid sites in each zeolite sample was determined via the reactive gas chromatography  
184 (RGC) method using isopropylamine (CH<sub>3</sub>CH(NH<sub>2</sub>)CH<sub>3</sub>) as the probe molecule. The selective

185 decomposition of isopropylamine adsorbate on Brønsted acid site ( $\text{CH}_3\text{CH}(\text{NH}_2)\text{CH}_3 \cdots \text{AlO}(\text{H})\text{Si}$ )  
186 in zeolites via Hoffmann elimination forms propylene and ammonia,  $\text{CH}_3\text{CH}(\text{NH}_2)\text{CH}_3 +$   
187  $\text{AlO}(\text{H})\text{Si} \rightarrow \text{CH}_3\text{CH}(\text{NH}_2)\text{CH}_3 \cdots \text{AlO}(\text{H})\text{Si} \rightarrow \text{CH}_2=\text{CHCH}_3 + \text{NH}_3 + \text{AlO}(\text{H})\text{Si}$ .<sup>25,26</sup> The  
188 quantification of propylene by a GC instrument determined the number of  $\text{AlO}(\text{H})\text{Si}$  sites in each  
189 zeolite sample. The experimental setup and reaction conditions for chemical titration of Brønsted  
190 acid site were the same as those reported by Abdelrahman, et al.<sup>26</sup>

191 The types of acid sites were identified by the recorded Fourier transform infrared (FTIR)  
192 spectra on a Nicolet iS-50R spectrometer with an associated Harrick Scientific Praying Mantis  
193 optical accessory and high temperature reaction chamber (HVC-DRP-5). In a typical run, the  
194 DRIFTS sample cell was filled with a zeolite sample that was pre-treated at 823 K for 6 h under  
195 flowing helium ( $\text{He}$ ,  $0.083 \text{ mL s}^{-1}$ ) in a furnace. The zeolite sample was then activated at 823  
196 K under the  $\text{He}$  flow ( $0.083 \text{ mL s}^{-1}$ ) for 1 h in the DRIFTS cell. After cooling the sample to 393  
197 K, a spectrum was recorded against the background spectrum of  $\text{KBr}$  powder measured under the  
198 same conditions. Afterwards, adsorption of pyridine was performed by flowing a mixed pyridine  
199 and  $\text{He}$  gas stream through the catalyst. Following adsorption, the sample was heated to 523 K  
200 under a flowing  $\text{He}$  to desorb the physisorbed pyridine, cooled to the temperature of 393 K, and  
201 then FTIR spectra were recorded in the range of  $4000\text{--}600 \text{ cm}^{-1}$  with 128 scans at an effective  
202 resolution of  $2 \text{ cm}^{-1}$ . The as-recorded FTIR spectra of adsorbed pyridine were used to determine  
203 the type and concentration of Brønsted and Lewis acid sites in the catalyst. Alternatively, the  
204 activated zeolite sample in the DRIFT cell was cooled to 303 K and then exposed to a mixed  
205 trideuteroacetonitrile ( $\text{CD}_3\text{CN}$ ) and argon ( $\text{Ar}$ ) gas stream using a bubbler with  $\text{Ar}$  as the carrier  
206 gas. After the excess  $\text{CD}_3\text{CN}$  was flushed out from the zeolite sample using a flowing  $\text{Ar}$  gas

207 (0.083 mL s<sup>-1</sup>), the spectra were collected at 2 cm<sup>-1</sup> resolution. The recorded FTIR spectra of  
208 CD3CN were used to analyze the Sn-site in each zeolite sample.

209 The acidity of the zeolite was further evaluated by ammonia temperature programmed  
210 desorption (NH<sub>3</sub>-TPD) using an Autosorb-iQ instrument (Quantachrome, ASIQM000-4)  
211 equipped with a thermal conductivity detector (TCD). In the NH<sub>3</sub>-TPD measurement, the zeolite  
212 sample (0.10 g) was loaded into a quartz cell and heated to 873 K at a rate of 0.05 K s<sup>-1</sup> under He  
213 (0.67 mL s<sup>-1</sup>) and maintained at this temperature for 1 h. After cooling to 423 K under the He  
214 stream, the sample was exposed to NH<sub>3</sub> stream (0.5 mL s<sup>-1</sup>, ultrapure, Airgas) for 0.5 h, and then  
215 back to the helium flow (0.5 mL s<sup>-1</sup>) for 2 h to remove NH<sub>3</sub> residue in the system. Lastly, the  
216 catalyst sample was ramped to 823 K at a ramp rate of 0.167 K s<sup>-1</sup>, and the NH<sub>3</sub> desorption  
217 profile was recorded.

#### 218 **Catalytic reaction for EMF synthesis from carbohydrates**

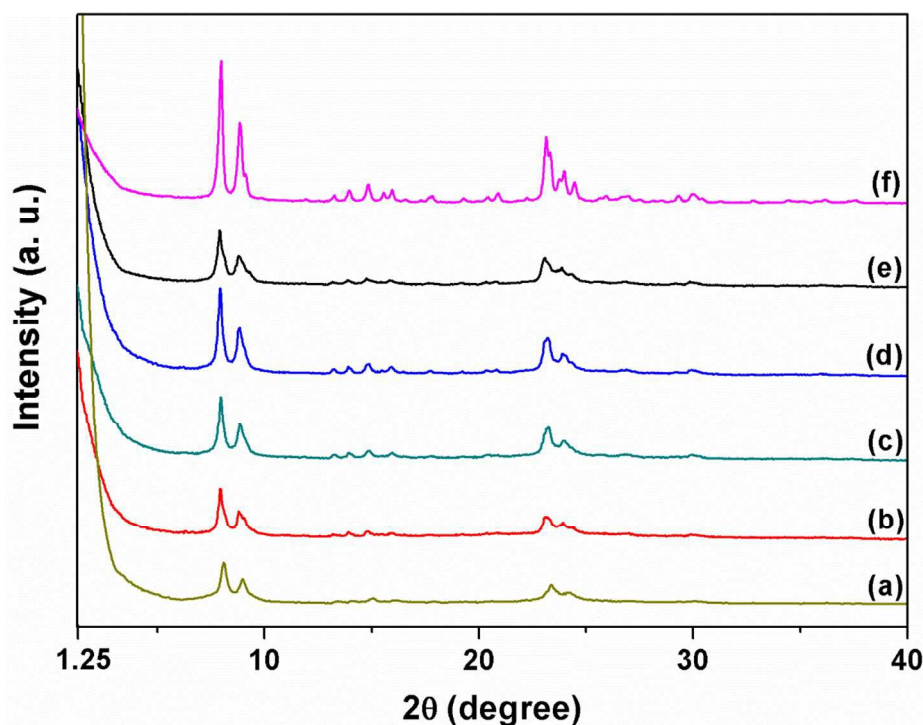
219 In a typical catalytic reaction, a 20 mL thick-walled glass reactor sealed with crimp tops  
220 (PTFE/silicone septum) was charged with glucose (0.090 g), zeolite catalyst (0.074 g), and  
221 ethanol (3 mL), respectively. The glass reactor was then heated to a desired temperature and the  
222 magnetic stirring was controlled at 600 rpm in all the catalysis experiment. After a certain  
223 reaction time, the reactor was quenched in an ice bath and the reaction mixture was sampled for  
224 composition analysis. A high performance liquid chromatography (HPLC, Agilent 1100)  
225 equipped with an Aminex HPX-87H column connected to an auto-sampler and a refractive index  
226 detector was used to calibrate and separate the reactant and products. During the measurement,  
227 the column was kept at 413 K with 0.005 M sulfuric acid at a flow rate of 0.5 mL min<sup>-1</sup> as the  
228 mobile phase. For comparison purpose, the same reaction and composition analysis conditions  
229 were applied to the fructose, sucrose, and inulin reactant in ethanol solvent, respectively. The

230 effect of types of reactants on the EMF production over MFI-Sn/Al zeolite catalysts was thus  
231 examined.

## 232 **Results and Discussion**

### 233 **Morphology and textural properties of MFI-Sn/Al zeolite catalysts**

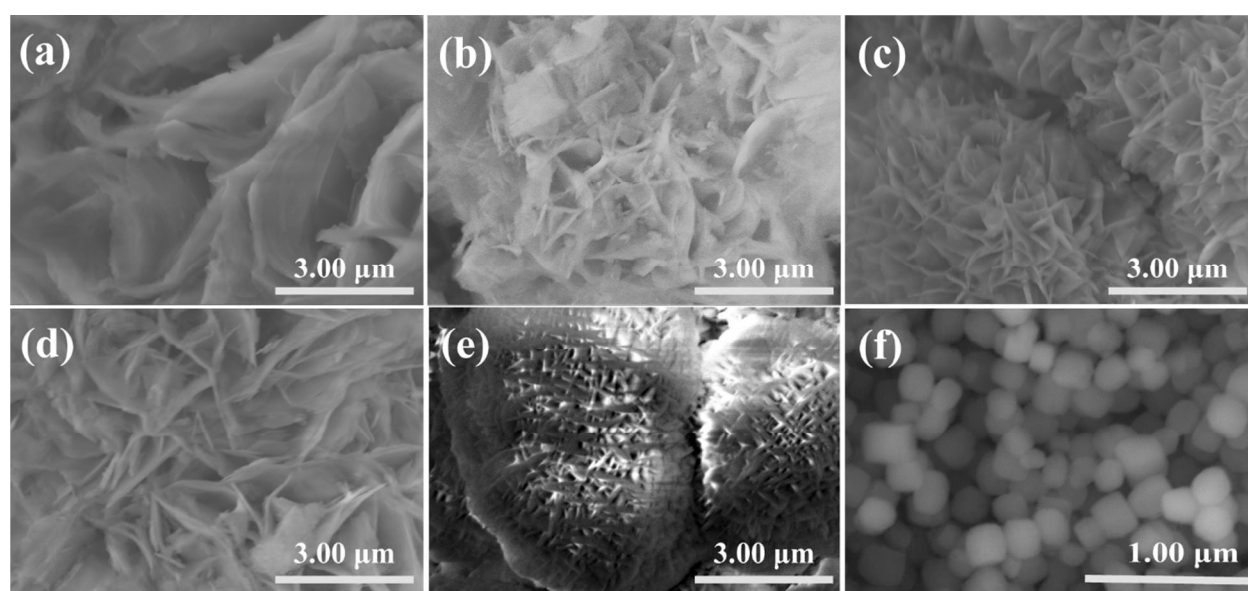
234 Fig. 1 shows XRD patterns of the synthesized hierarchical lamellar MFI-Sn/Al zeolite catalysts.  
235 For comparison purpose, the XRD patterns of lamellar MFI that only contains Al sites (MFI-  
236 Sn/Al ( $\infty/100$ )) and conventional microporous MFI that comprises of both Sn and Al sites (C-  
237 MFI-Sn/Al (100/100)) are included. As indicated in Fig. 1, all the MFI-Sn/Al zeolite samples  
238 exhibit similar diffraction patterns, resembling the characteristics of crystalline MFI  
239 zeolite.<sup>21,27,28</sup> This result confirms the successful synthesis of hierarchical lamellar MFI in the  
240 presence of both Sn and Al species in the synthesis gels. The absence of small-angle diffraction  
241 peaks in Fig. 1 suggests that long-range ordering of the layered zeolitic structure does not exist in  
242 the hierarchical lamellar MFI-Sn/Al zeolites. A comparison for the peak intensity between the  
243 MFI-Sn/Al samples and C-MFI-Sn/Al (100/100) shows that the diffraction peak intensities of the  
244 former samples are all relatively lower than the latter one. This is mainly caused by the small  
245 framework thickness along the *b*-axis direction in the hierarchical lamellar MFI-Sn/Al zeolites  
246 compared to that in the three dimensional microporous C-MFI-Sn/Al (100/100) zeolite.<sup>20</sup>



247  
248 **Fig. 1** XRD patterns of (a) MFI-Sn/Al ( $\infty/100$ ), (b) MFI-Sn/Al (50/50), (c) MFI-Sn/Al (100/25),  
249 (d) MFI-Sn/Al (100/50), (e) MFI-Sn/Al (100/100) and (f) C-MFI-Sn/Al (100/100), respectively.

250 The morphologies of the hierarchical lamellar MFI-Sn/Al zeolites together with C-MFI-  
251 Sn/Al (100/100) and MFI-Sn/Al ( $\infty/100$ ) samples are shown by the SEM images in Fig. 2 and  
252 Fig. S1 in the supplementary information. All the MFI-Sn/Al zeolites (Figs. 2(a)-(e)) are  
253 comprised of interweaved platelet-like structure that formed flower-like aggregates with irregular  
254 sizes (Fig. S1), while the C-MFI-Sn/Al (100/100) sample is composed of uniform but irregular  
255 shaped particles, whose sizes are in the range of 150 – 200 nm (Fig. 2(f)). A closer examination  
256 on the MFI-Sn/Al zeolite samples shows that the width and thickness of the platelet-like  
257 structure decreases with increasing Al content in the synthesis recipe (Figs. 2a-b-c). Moreover,  
258 the platelet-like structures change from curved to straight ones with increasing Al content.  
259 Similarly, the increase in Sn content in the synthesis recipe decreases the thickness of the zeolite  
260 platelet-like structure in the MFI-Sn/Al samples (refer to Figs. 2b-d). The effect of Si/Al and

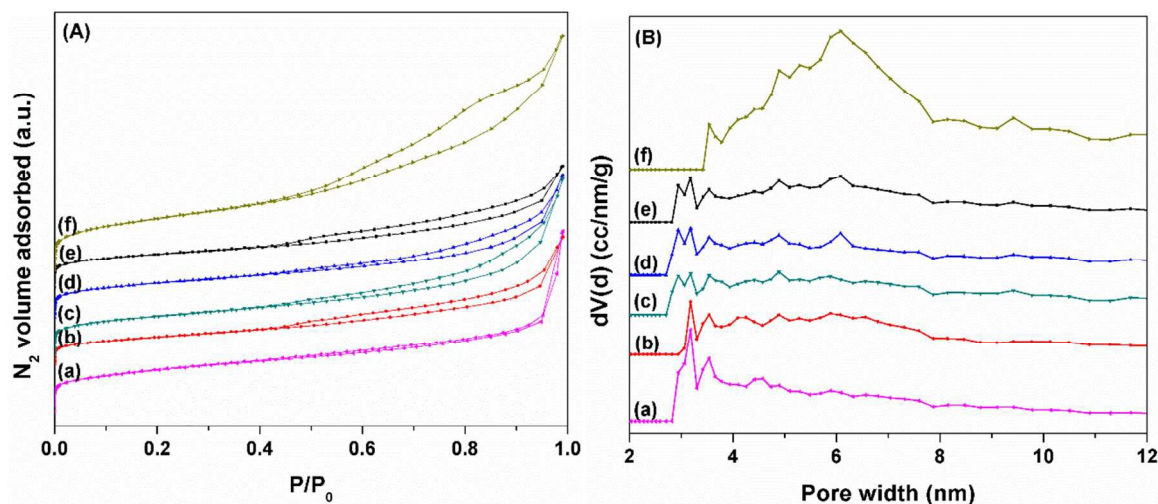
261 Si/Sn ratios in the synthesis recipe on the morphology of derived MFI-Sn/Al zeolites is the same  
262 as that observed by Machoke et al<sup>29</sup> on synthesis of multilamellar MFI under static condition.  
263 The introduction of aluminum and/or tin into the lamellar zeolite synthesis recipe leads to defects  
264 in zeolite nanosheet structures, which consequently affect the growth of nanosheets along the a-c  
265 plane. Therefore, more randomly oriented and smaller sized zeolite nanosheets are formed in the  
266 crystallization process, which results in the thinner and straighter zeolite plates from the  
267 synthetic gels containing higher aluminum and/or tin contents.



268  
269 **Fig. 2** SEM images of (a) MFI-Sn/Al (100/100), (b) MFI-Sn/Al (100/50), (c) MFI-Sn/Al  
270 (100/25), (d) MFI-Sn/Al (50/50), (e) MFI-Sn/Al ( $\infty$ /100) and (f) C-MFI-Sn/Al (100/100),  
271 respectively.

272  $N_2$  adsorption-desorption isotherms were used to study the textural properties of the MFI-  
273 Sn/Al zeolite samples. The textural parameters of each sample are included in Table S1 of the  
274 supplementary information. Fig. 3A illustrates that all the synthesized hierarchical lamellar MFI-  
275 Sn/Al zeolites exhibit type-IV isotherms with hysteresis loops corresponding to capillary  
276 condensation in mesopores.<sup>21,30</sup> Particularly, at low relative pressures ( $P/P_0 < 0.45$ ), the

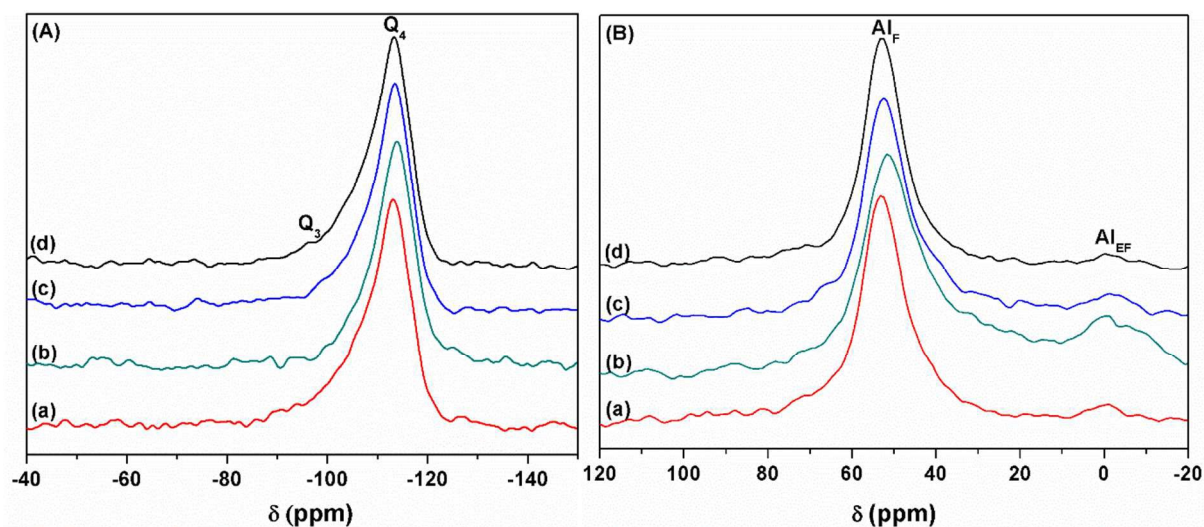
277 isotherms of these zeolites are similar and comparable to that of C-MFI-Sn/Al (100/100) zeolite.  
278 This suggests all the synthesized MFI-Sn/Al samples have similar micropore structures. At high  
279 relative pressures ( $P/P_0 > 0.45$ ), the isotherms of the MFI-Sn/Al samples show hysteresis loops,  
280 different from that of C-MFI-Sn/Al (100/100). For all the MFI-Sn/Al samples, the hysteresis  
281 loops in their isotherms are relatively narrow and flat, which indicates these materials have  
282 disordered mesopores and broad pore size distributions.<sup>31,32</sup> Fig. 3B shows the nonlocal density  
283 functional theory (NLDFT) pore size distributions of all MFI-Sn/Al samples. As suggested from  
284 the shape of hysteresis loops in their isotherms, the MFI-Sn/Al (100/100), MFI-Sn/Al (50/50),  
285 MFI-Sn/Al (100/50), and MFI-Sn/Al (100/25) zeolites have broad mesopore size distributions. In  
286 contrast, the C-MFI-Sn/Al (100/100) zeolite does not have significant mesoporosity.



287  
288 **Fig. 3** N<sub>2</sub> isotherms (A) and the corresponding NLDFT pore size distributions (B) as determined  
289 from adsorption branch of (a) C-MFI-Sn/Al (100/100), (b) MFI-Sn/Al (50/50), (c) MFI-Sn/Al  
290 (100/25), (d) MFI-Sn/Al (100/50), (e) MFI-Sn/Al (100/100) and (f) MFI-Sn/Al ( $\infty$ /100),  
291 respectively.

292 Solid state NMR was employed to investigate the local bonding environment of Si and Al  
293 species in the MFI-Sn/Al zeolite catalysts. Figs. 4A and 4B show the <sup>29</sup>Si single pulse (SP) and

294  $^{27}\text{Al}$  NMR spectra of the MFI-Sn/Al (100/100), MFI-Sn/Al (50/50), MFI-Sn/Al (100/50), and  
 295 MFI-Sn/Al (100/25) zeolites, respectively. In Fig. 4A, one well-resolved peak at -113 ppm and  
 296 one shoulder peak at -103 ppm can be observed. These two peaks correspond to the  
 297 crystallographically nonequivalent  $\text{Q}^4$  tetrahedral sites ( $\text{Q}^n$  stands for  $\text{X}_{4-n}\text{Si}[\text{OSi}]_n$ )<sup>33-36</sup> and  $\text{Q}^3$   
 298 sites that arise from the silanol groups on the zeolite surface,<sup>23,37</sup> respectively. The similarity of  
 299  $^{29}\text{Si}$  SP NMR spectra of MFI-Sn/Al zeolites suggests similar local bonding environments exist in  
 300 these samples. In Fig. 4B, the two peaks (at 55 ppm and 0 ppm) in the  $^{27}\text{Al}$  MAS NMR spectra  
 301 were observed. The peak at 55 ppm is due to the tetrahedrally coordinated framework aluminum  
 302 ( $\text{Al}_\text{F}$ ), whereas the peak around 0 ppm is due to an octahedral coordination typical of extra-  
 303 framework Al ( $\text{Al}_\text{EF}$ ).<sup>38-40</sup> The percentages of the  $\text{Al}_\text{EF}$  sites in MFI-Sn/Al (50/50), MFI-Sn/Al  
 304 (100/25), MFI-Sn/Al (100/50), and MFI-Sn/Al (100/100) samples were calculated from the  
 305 intensities of the peak around 0 ppm over the peak around 55 ppm, which are 3.6%, 8.1%, 4.4%  
 306 and 2.0%, respectively. Obviously, the higher Al content in the synthesis led to higher  
 307 proportions of  $\text{Al}_\text{EF}$  in MFI-Sn/Al zeolites. When the concentration of Al was the same, the one  
 308 with higher Sn content in the synthesis recipe resulted in a higher proportion of  $\text{Al}_\text{EF}$  in the as-  
 309 obtained MFI-Sn/Al samples.



310

311 **Fig. 4** Solid-state  $^{29}\text{Si}$  MAS NMR (A) and  $^{27}\text{Al}$  MAS NMR (B) spectra of hierarchical lamellar  
312 MFI-Sn/Al zeolite samples: (a) MFI-Sn/Al (50/50), (b) MFI-Sn/Al (100/25), (c) MFI-Sn/Al  
313 (100/50), and (d) MFI-Sn/Al (100/100), respectively.

#### 314 **Composition and acidity of MFI-Sn/Al zeolite catalysts**

315 The tin (Sn) and aluminum (Al) contents of the MFI-Sn/Al zeolite samples were analyzed by  
316 ICP-AES technique, represented by Si/Sn and Si/Al ratios, as shown in Table S2 of the  
317 supplementary information. The Sn and Al concentrations of the synthesized MFI-Sn/Al samples  
318 are generally higher than those determined from the synthesis recipe. Table 1 lists the  
319 concentrations of Al and Sn sites determined by elemental analysis and the concentration of  
320 Brønsted acid sites measured by RGC method. The concentration of Al sites is higher than  
321 Brønsted acid sites, suggesting that there is a considerable amount of non-framework Al in the  
322 synthesized MFI-Sn/Al zeolite samples. If we assume all the Al species that could not be  
323 detected by the RGC method as Lewis acid site ( $L_{(\text{Al})}$ ), the ratio of the Brønsted to Lewis (Al)  
324 acid site can be calculated, as shown by entry 6 in Table 1. The overall Brønsted to Lewis acid  
325 site ratio (entry 7 in Table 1) in each zeolite sample can also be evaluated by division of Brønsted  
326 acid sites with the sum of Lewis (Al) acid and Sn sites. Apparently, the increase in Al or Sn  
327 content in the hydrothermal synthesis increased more Lewis acid sites compared to Brønsted acid  
328 sites in the MFI-Sn/Al samples.

329 **Table 1** Concentration of Sn, Al and acid sites in MFI-Sn/Al zeolite catalysts.

Zeolite	Sn <sup>a</sup> (mmol/g)	Al <sup>a</sup> (mmol/g)	Brønsted acid site <sup>b</sup> (mmol/g)	Lewis (Al) acid site ( $L_{(\text{Al})}$ ) <sup>c</sup> , (mmol/g)	Brønsted/Lewis (Al) acid site ratio <sup>d</sup> ( $I_{\text{B}}/I_{\text{L}(\text{Al})}$ )	Brønsted/Lewis (Al + Sn) acid site ratio <sup>e</sup> ( $I_{\text{B}}/I_{\text{L}(\text{Al}+\text{Sn})}$ )	Brønsted/Lewis acid site ratio <sup>f</sup> ( $I_{\text{B}}/I_{\text{L}}$ )
MFI-Sn/Al (100/100)	0.219	0.245	0.141	0.104	1.351	0.436	0.989
MFI-Sn/Al (100/50)	0.317	0.505	0.239	0.266	0.895	0.410	0.893
MFI-Sn/Al (100/25)	0.299	0.794	0.274	0.520	0.528	0.334	0.744

MFI-Sn/Al (50/50)	0.523	0.438	0.121	0.317	0.379	0.144	0.464
MFI-Sn/Al (∞/100)	0	0.228	0.159	0.069	-	-	-

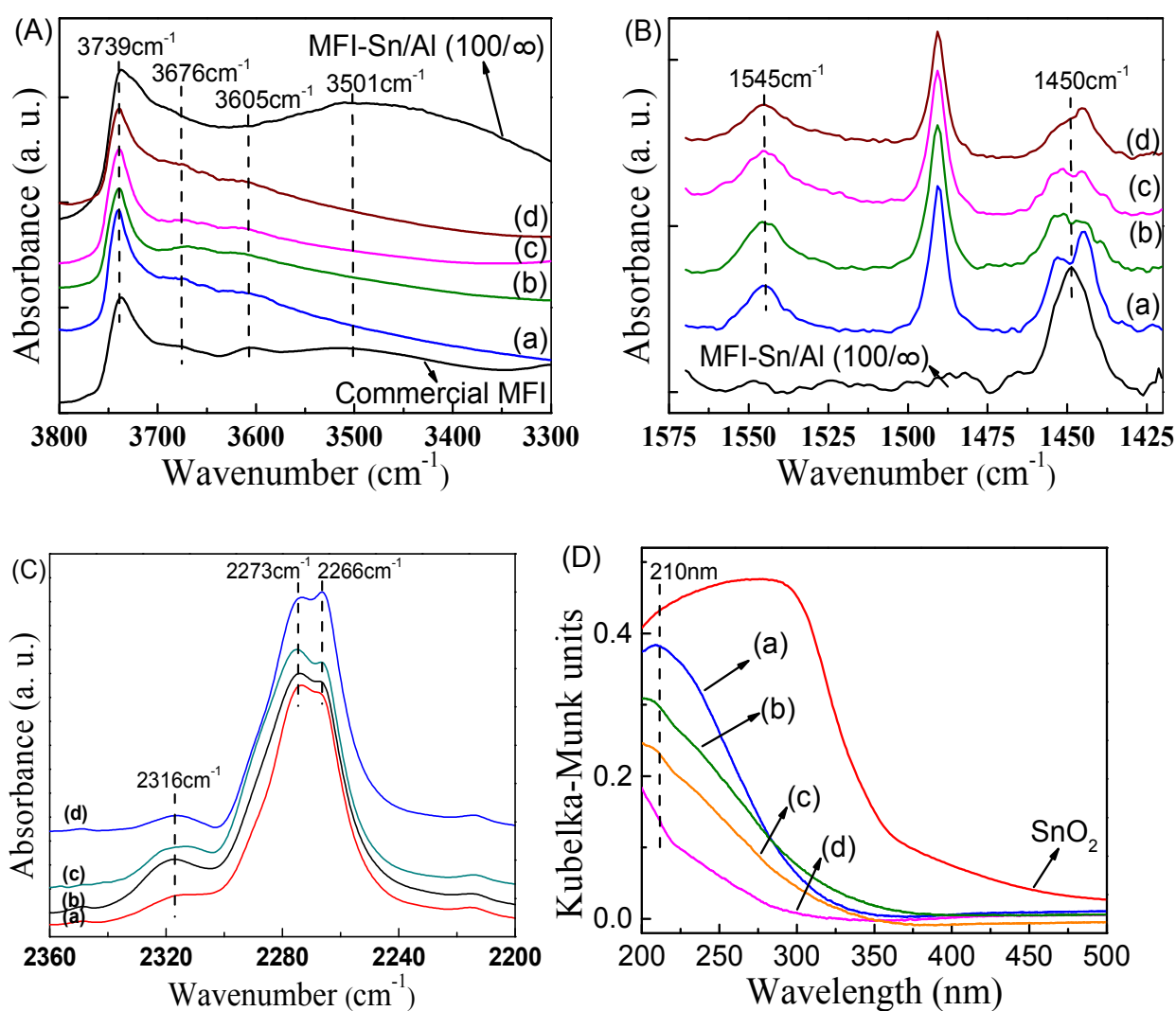
330 <sup>a</sup> Calculated from elemental analysis (ICP-AES); <sup>b</sup> Determined from RGC by selective decomposition of isopropyl  
 331 amine on Brønsted acid sites; <sup>c</sup> Determined from deduction of concentration of Brønsted acid sites determined by  
 332 RGC from Al concentration measured by elemental analysis; <sup>d</sup> Calculated by ratio of data in column 4 relative to  
 333 that in column 5; <sup>e</sup> Calculated by ratio of data in column 4 relative to the sum of data in columns 2 and 5; <sup>f</sup> Evaluated  
 334 by FTIR spectra of adsorbed pyridine.  $I_B/I_L$  is the ratio of peak intensity of  $1545\text{ cm}^{-1}$  relative to that of  $1450\text{ cm}^{-1}$ .  
 335

336 To understand the types of acidity, the FTIR spectra of the OH-stretching mode ( $\nu(\text{OH})$ ) and  
 337 adsorbed pyridine in the MFI-Sn/Al samples were recorded, as presented in Fig. 5(A) and (B),  
 338 respectively. In Fig. 5(A), there are four peaks centered around  $3739\text{ cm}^{-1}$ ,  $3676\text{ cm}^{-1}$ ,  $3605\text{ cm}^{-1}$ ,  
 339 and  $3501\text{ cm}^{-1}$ , in sequence, which are associated with terminal silanol (Si-OH) groups, Lewis  
 340 acidic or non-acidic extraframework Al-OH, Brønsted acid sites (Si-O(H)-Al), and hydrogen-  
 341 bonded internal silanol (Si-OH) groups.<sup>41-45</sup> In the absence of Al in MFI-Sn/Al (100/∞) zeolite,  
 342 the peak of Si-O(H)-Al does not exist, in contrast to the  $3605\text{ cm}^{-1}$  peak in all other MFI-Sn/Al  
 343 samples. The same trend is observed in Al-OH sites in all these samples. The increase in Al  
 344 (sample (b)-(d) or Sn (sample (a) and (c)) content increased the Al-OH and (Si-O(H)-Al) sites, as  
 345 indicated by increasing intensity of  $3676\text{ cm}^{-1}$ ,  $3605\text{ cm}^{-1}$  peaks. The control sample, commercial  
 346 MFI, and the conventional microporous MFI-Sn/Al (100/∞) both contain a big peak at  $3500\text{ cm}^{-1}$ ,  
 347 indicating the presence of internal Si-OH groups in these samples. The hierarchical MFI-Sn/Al,  
 348 apparently, have quite low amount of such internal groups. Fig. 5(B) presents the FTIR spectra  
 349 of adsorbed pyridine on zeolites, which hints the relative quantity of Brønsted to Lewis acid sites  
 350 in the MFI-Sn/Al samples.<sup>46</sup> MFI-Sn/Al (50/50), MFI-Sn/Al (100/25), MFI-Sn/Al (100/50) and  
 351 MFI-Sn/Al (100/100) all showed characteristic peaks for Brønsted ( $1545\text{ cm}^{-1}$ ) and Lewis ( $1450$   
 352  $\text{ cm}^{-1}$ ) acid sites. MFI-Sn/Al (100/∞) only showed the peak of Lewis acid sites due to the absence  
 353 of Al in the structure. The difficulty in determining accurate molar extinction coefficients of

354 solid acid materials in DRIFT mode restricts our capability of calculating the accurate number of  
355 Brønsted and Lewis acid sites in each sample.<sup>47,48</sup> The intensities of the signals in Fig. 5(B), due  
356 to both types of acid sites, are proportional to their concentrations. Therefore, we conducted  
357 semi-quantitative analyses of the ratio of Brønsted to Lewis acid sites in MFI-Sn/Al zeolites by  
358 calculating the intensity ratio of Brønsted relative to the Lewis ( $I_B/I_L$ ) acid sites in these samples.  
359 As listed in Table 1, the  $I_B/I_L$  decreases with increasing Al content from samples (b)-(d). The  
360 increase in Sn content from samples (a) and (c) enhanced the Lewis acidity. These results are  
361 consistent with the type of acidity determination by the combination of elemental analysis and  
362 RGC measurement in Table 1.

363 FTIR spectroscopy of adsorbed deuterated acetonitrile can be used for characterization of  
364 the framework and extra-framework Lewis acid Sn sites in Sn-Beta<sup>49,50</sup> or Sn-MFI<sup>51</sup> zeolites. We  
365 also used this technique to understand the structure of Sn sites existing in the synthesized MFI-  
366 Sn/Al zeolites. As shown in Fig. 5(C), three peaks at 2266, 2273 and 2316  $\text{cm}^{-1}$  are observed,  
367 which are assigned to the C-N stretching vibration of the adsorbed deuterated acetonitrile<sup>49</sup>. The  
368 band at 2266 and 2273  $\text{cm}^{-1}$  corresponds to the deuterated acetonitrile physisorbed and adsorbed  
369 on silanol groups. The band at 2316  $\text{cm}^{-1}$  can be assigned to the stronger deuterated acetonitrile  
370 adsorption on Lewis acid sites<sup>49</sup>. According to the previous report<sup>50</sup>, the features near 2316  $\text{cm}^{-1}$   
371 are clearly associated with framework Sn sites, which confirmed the presence of framework Sn  
372 in the zeolite structures. Furthermore, the structure of Sn sites was evaluated by the UV-vis-DRS  
373 spectra, as shown in Fig. 5(D). The absorbance around 210 nm was observed for all the MFI-  
374 Sn/Al samples, showing the presence of isolated, tetrahedral  $\text{Sn}^{4+}$  species within the zeolite  
375 framework. The increase in Sn content in the synthesis increased the  $\text{Sn}^{4+}$  sites in the resultant  
376 MFI-Sn/Al zeolites, as indicated by the sample (a) and (c) in Fig. 5(D). The increase in Al

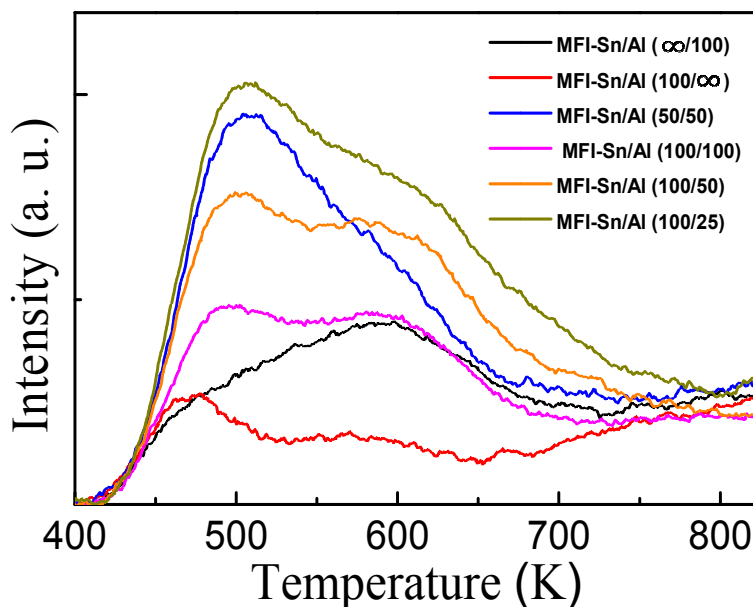
377 content in zeolite synthesis affected the incorporation of Sn sites into the framework, as reflected  
 378 by the increase in 210 nm peak intensity from sample (b), (c) and (d). Apparently, no Sn oxide is  
 379 observed in all MFI-Sn/Al zeolite samples, as indicated by the absence of characteristic peak of  
 380 SnO<sub>2</sub> sample.



383 **Fig. 5** (A) DRIFTS spectra of MFI-Sn/Al zeolites; FTIR spectra of pyridine (B) and deuterated  
 384 acetonitrile (C) adsorbed on the MFI-Sn/Al zeolites; and (D) DR-UV-vis spectra of MFI-Sn/Al  
 385 samples, respectively. (Denotation in each figure: (a) MFI-Sn/Al (50/50), (b) MFI-Sn/Al (100/25),  
 386 (c) MFI-Sn/Al (100/50) and (d) MFI-Sn/Al (100/100). MFI-Sn/Al (100/∞) stands for

387 conventional microporous MFI comprised of only Sn sites. The commercial MFI with Si/Al ratio  
388 of 40 (Supplier No. 45882-36) in Fig. 5(A) and SnO<sub>2</sub> (Supplier No. 44606-18) in Fig. 5(D) were  
389 purchased from Alfa Aesar.)

390 The acidity of the MFI-Sn/Al zeolite catalysts were further characterized by the NH<sub>3</sub>-TPD  
391 measurement, and the results are shown in Fig. 6. Two desorption peaks located in the  
392 temperature range of 400-550 K (low temperature desorption peak) and 550-750 K (high  
393 temperature desorption peak), respectively, are observed in all the tested zeolite samples. It has  
394 been generally reported that the low temperature peak is associated with the physical and Lewis  
395 acid site adsorption of NH<sub>3</sub>, while the high temperature desorption peak is assigned to the  
396 adsorption of NH<sub>3</sub> on the Brønsted acid sites in the catalysts<sup>52-54</sup>, although caution must be paid  
397 since desorption of NH<sub>3</sub> from non-acidic sites in catalysts can take place over a wide  
398 temperature range.<sup>55,56</sup> Additionally, the intensity is correlated to the quantity of acid sites in the  
399 zeolite catalysts.<sup>57</sup> Fig. 6 shows that the low and high temperature desorption peaks are increased  
400 with increasing Al sites from MFI-Sn/Al (100/∞), MFI-Sn/Al (100/100), MFI-Sn/Al (100/50) to  
401 MFI-Sn/Al (100/25) materials. The increase in Sn sites mainly increases the low temperature  
402 peak, as the zeolite samples transit from MFI-Sn/Al (∞/100) to MFI-Sn/Al (100/100) and MFI-  
403 Sn/Al (50/50) to MFI-Sn/Al (100/50). The results suggest that Al in the MFI-Sn/Al zeolites led  
404 to both Lewis and Brønsted acidity, while Sn-site predominately contributes to the Lewis acidity.



405  
406 **Fig. 6** NH<sub>3</sub>-TPD profiles of MFI-Sn/Al zeolites with different Si/Al and Si/Sn ratios. (MFI-Sn/Al  
407 (∞/100) and MFI-Sn/Al (100/∞) stand for the conventional microporous MFI zeolites containing  
408 only Al and Sn sites, respectively.)

#### 409 **Reaction cascade for EMF synthesis from carbohydrates over MFI-Sn/Al zeolite catalysts**

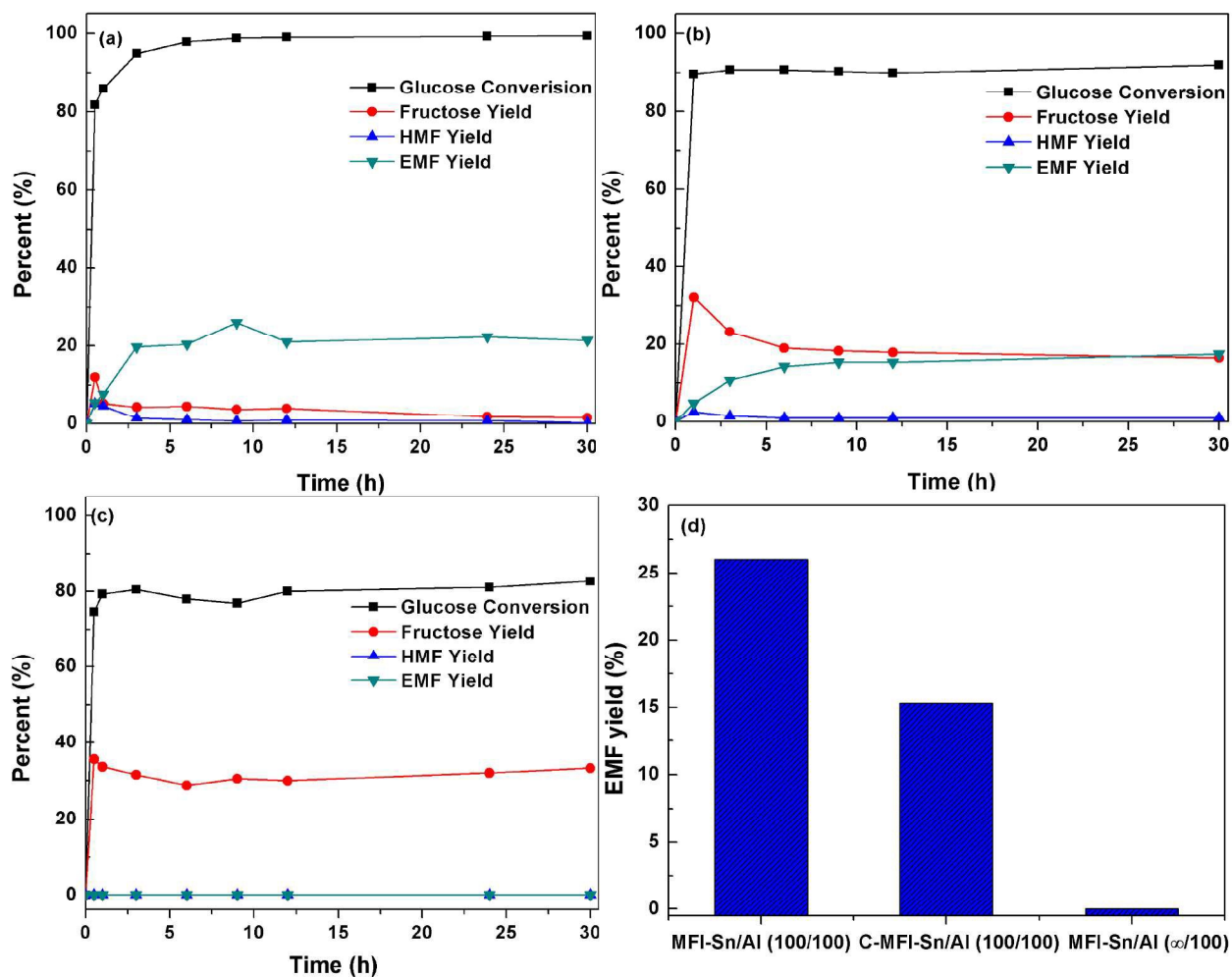
410 As shown in Scheme 1, the EMF synthesis from glucose carbohydrate occurs via a three-step  
411 reaction cascade, in which the first step is isomerization of glucose into fructose and the next two  
412 steps are dehydration of fructose to HMF and etherification of HMF to EMF final product. The  
413 first step reaction can be catalyzed by the Lewis acidic Sn sites and the last two steps can take  
414 place over the Brønsted acidic Al–O(H)–Si sites in the MFI-Sn/Al zeolite catalysts. The acidity  
415 characterizations in Section 3.2 indicate the co-existence of both Sn and Al sites, *i.e.*, both Lewis  
416 and Brønsted acid sites, in the MFI-Sn/Al zeolites. We expect that they are efficient catalysts for  
417 this three-step reaction cascade. Moreover, the morphological and textural property  
418 characterizations in Section 3.1 indicates the presence of mesoporosity in the synthesized MFI-  
419 Sn/Al zeolites, which could be beneficial for the reaction cascade compared to the conventional

420 microporous zeolite analogue. We, therefore, studied the performance of the MFI-Sn/Al zeolite  
421 catalysts in EMF synthesis from carbohydrate reactants. The effects of catalyst structure, reaction  
422 temperature, catalyst acidity and carbohydrate reactant type on EMF synthesis were examined in  
423 sequence via a series of catalytic reactions. The reaction conditions used for EMF synthesis from  
424 glucose reactant over MFI-Sn/Al (100/100) catalyst at 413 K were used as the base case for  
425 comparison. Individual experimental variables were changed, and the effects of changing these  
426 variables were investigated by comparing the catalysis data to that obtained with the standard  
427 conditions, as discussed below.

#### 428 **EMF synthesis from glucose over MFI-Sn/Al (100/100), C-MFI-Sn/Al (100/100) and MFI-** 429 **Sn/Al ( $\infty$ /100) catalysts**

430 The synthesis of EMF from glucose was firstly tested over the MFI-Sn/Al (100/100), C-MFI-  
431 Sn/Al (100/100), and MFI-Sn/Al ( $\infty$ /100) zeolite catalysts. Figs. 7a-c show the glucose  
432 conversion and product yields versus the reaction time over each catalyst. It should be noted that  
433 the products are mainly comprised of fructose, HMF and EMF in the glucose-to-EMF conversion,  
434 and thus only these major products were analyzed in the present study. Fig. 7d shows the EMF  
435 yield at the reaction time of 9 h over each tested catalyst. As demonstrated in Figs. 7a-c, the  
436 glucose conversion was higher in MFI-Sn/Al (100/100) than C-MFI-Sn/Al (100/100), so did the  
437 EMF yield (Fig. 7d). A closer examination on the kinetic data (e.g., reaction time: < 5 h) in Figs.  
438 7a and b shows that the EMF formation took place at a much faster rate in MFI-Sn/Al (100/100)  
439 than C-MFI-Sn/Al (100/100) catalyst. These results indicate that mesoporosity in the hierarchical  
440 lamellar MFI zeolite plays an important role in enhancing this three-step reaction cascade. As  
441 reported previously, the Stokes diameter of glucose is 0.73 nm,<sup>58</sup> larger than the micropore sizes  
442 of MFI zeolite. As a result, the reaction mainly takes place on the external surface of

443 conventional C-MFI-Sn/Al (100/100) zeolite. The presence of mesopores in MFI-Sn/Al (100/100)  
444 apparently promotes the access of reactant to acid sites in interior of MFI-Sn/Al (100/100)  
445 zeolite. The mesopores also enhance the transport of reactant onto or product (or reaction  
446 intermediate) away from the active sites in the catalyst in these three steps in the reaction cascade.  
447 The sole presence of Al sites in the hierarchical lamellar MFI zeolite (MFI-Sn/Al ( $\infty$ /100)) also  
448 enabled glucose conversion, but the conversion was lower than MFI-Sn/Al (100/100) and  
449 produced nearly zero EMF production (Figs.7c and d). Both glucose conversion and EMF yield  
450 suggest the efficiency of Lewis Sn sites in catalysts for glucose isomerization, as well as the  
451 dehydration and etherification steps in the three-step reaction cascade. Additionally, the  
452 comparison between the performances of MFI-Sn/Al (100/100) and MFI-Sn/Al ( $\infty$ /100) also  
453 suggests the efficiency of the cooperative catalysis offered from both types of acid sites in this  
454 three-step reaction cascade.

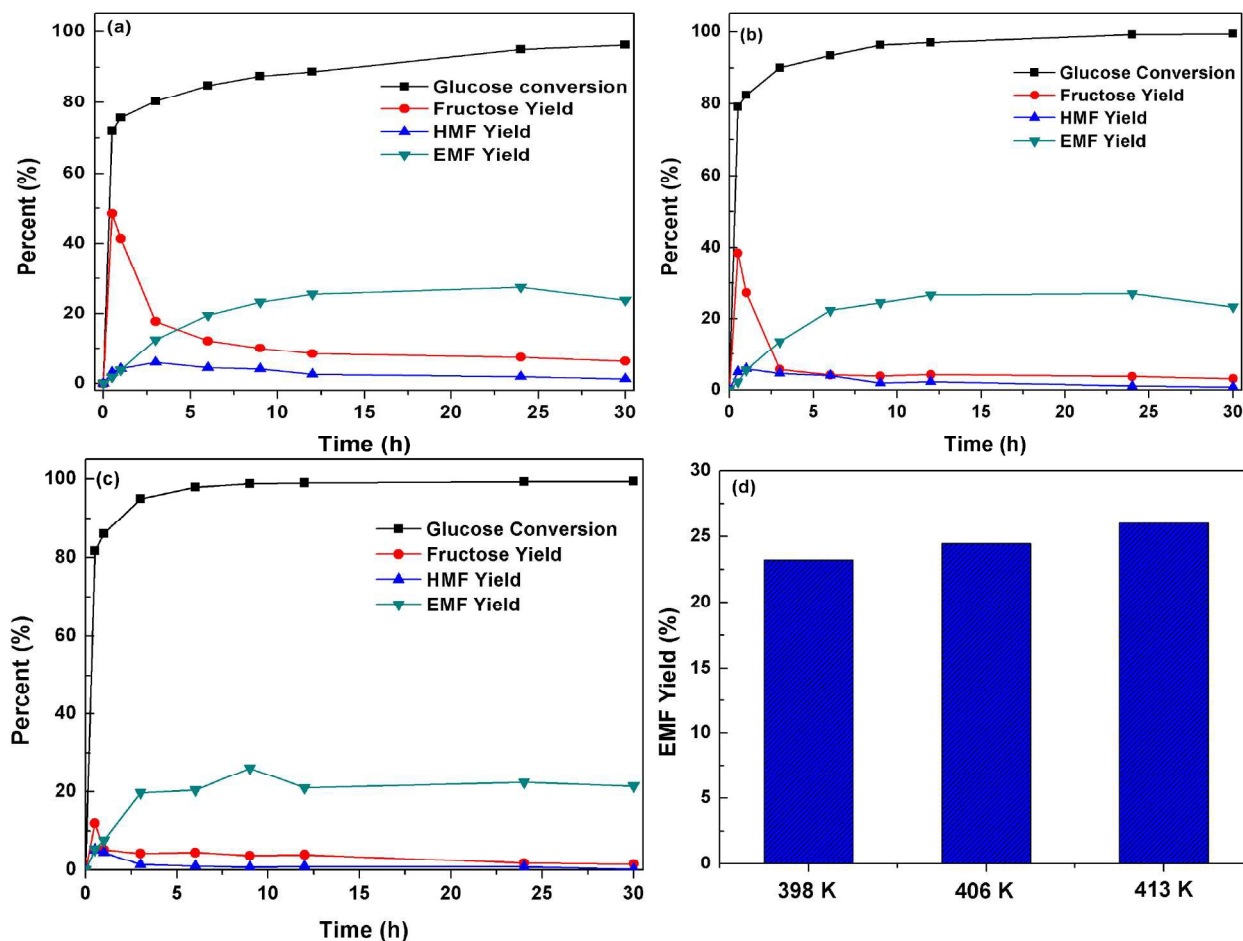


455  
 456 **Fig. 7** Catalytic conversion of glucose to EMF over (a) MFI-Sn/Al (100/100), (b) C-MFI-Sn/Al  
 457 (100/100) and (c) MFI-Sn/Al ( $\infty$ /100), respectively, versus reaction time. (d) shows the EMF  
 458 yield at reaction time of 9 h across these three zeolite catalysts. (reaction condition: glucose:  
 459 0.090 g; zeolite: 0.074 g; temperature: 413 K; ethanol: 3 mL).

460 **Effect of reaction temperature on EMF synthesis from glucose over MFI-Sn/Al (100/100)**  
 461 **catalyst**

462 The effect of reaction temperature on glucose conversion to EMF over the MFI-Sn/Al zeolite  
 463 catalysts was examined by employing the MFI-Sn/Al (100/100) catalyst at the reaction  
 464 temperature of 398 K, 406 K, and 413 K, respectively. Fig. 8 shows the glucose conversion and

465 product yields as a function of the reaction time (Figs. 8a-c) together with the EMF yield at the  
466 reaction time of 9 h (Fig. 8d) at these three reaction temperatures. By increasing the reaction  
467 temperature from 398 K to 413 K, the rate of glucose conversion increased, so did the fructose  
468 conversion and EMF production (refer to reaction time of 0-5 h in Figs. 8a-c). The changes of  
469 HMF yields follow the same trend of fructose. This indicates the successive three-step reaction  
470 nature in glucose-to-EMF reaction cascade, besides the endothermic nature of these three  
471 reaction steps. The maximum EMF yields in the course of this reaction are slightly increased  
472 with an increase in the reaction temperature. As shown in Fig. 8d, the EMF yield was increased  
473 from 23.2% to 24.5% to 26.0% when the reaction temperature was increased from 398 K to 406  
474 K and then to 413 K. These results indicate that higher temperature increases the conversion of  
475 glucose reactant and the successive step of dehydration of fructose in the three-step reaction  
476 cascade.



477  
 478 **Fig. 8** Effect of reaction temperature ((a) 398 K, (b) 406 K, and (c) 413 K, respectively) on  
 479 catalytic conversion of glucose to EMF over MFI-Sn/Al (100/100). (d) shows the maximum  
 480 EMF yield at the reaction process at these three temperatures. (reaction condition: glucose: 0.090  
 481 g; zeolite: 0.074 g; ethanol: 3 mL).

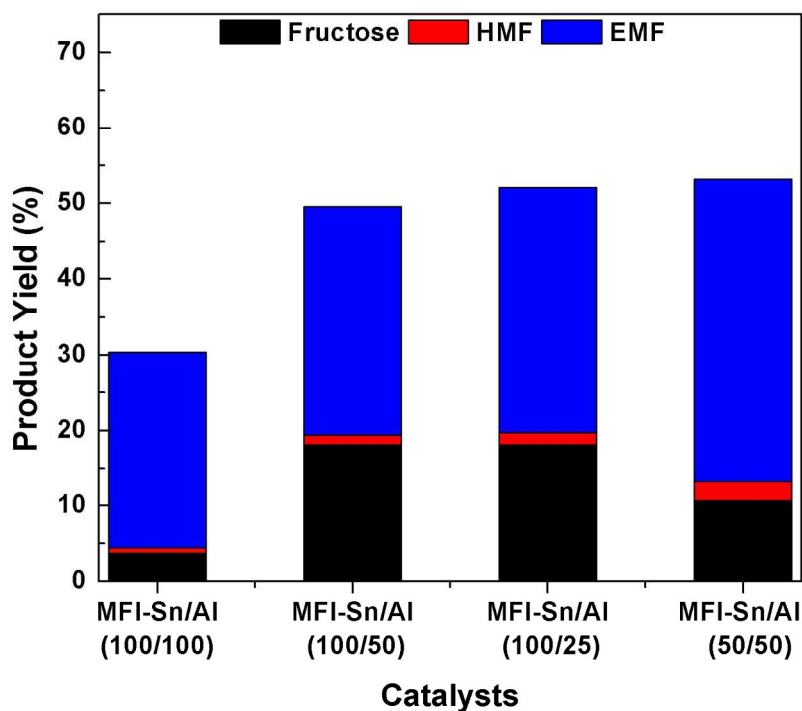
#### 482 Effect of zeolite acidity on EMF synthesis from glucose over MFI-Sn/Al catalysts

483 The influences of Sn and Al contents (*i.e.*, acidity, represented by Si/Sn and Si/Al ratios) in MFI-  
 484 Sn/Al zeolite catalysts on their catalytic performances in the glucose-to-EMF reaction was  
 485 studied at 413 K. Fig. 9 shows the product yields from the reaction over MFI-Sn/Al (100/100),  
 486 MFI-Sn/Al (100/50), MFI-Sn/Al (100/25), and MFI-Sn/Al (50/50) catalysts, respectively. As  
 487 indicated in this figure, all the MFI-Sn/Al zeolites enabled EMF, HMF and fructose production.

488 The yields of these three products follow the order of EMF > fructose > HMF in each catalyst,  
489 suggesting the etherification of HMF to EMF happened much faster than dehydration of fructose  
490 in this reaction cascade. Fig. 9 also shows that the HMF and EMF yields from this reaction  
491 cascade increases in the order of MFI-Sn/Al (100/100) < MFI-Sn/Al (100/50) < MFI-Sn/Al  
492 (100/25) << MFI-Sn/Al (50/50). The fructose yield also follows the same order as that of EMF  
493 and HMF over the MFI-Sn/Al (100/100), MFI-Sn/Al (100/50) and MFI-Sn/Al (100/25) catalysts  
494 that have similar number of Sn sites but different Al sites. The increase in Al content increases  
495 Brønsted acidity of the MFI-Sn/Al catalysts, which benefits etherification of HMF to EMF  
496 reaction step. Additionally, this acidity enhances dehydration of fructose to HMF and  
497 isomerization of glucose to fructose reaction steps. It should be noted that the glucose conversion  
498 happened at a slower rate with increasing Al content in MFI-Sn/Al catalysts (refer to Figs. S2a-  
499 b-c in Section S2 of the Supplementary Information). The controversy between the glucose  
500 conversion and fructose/HMF/EMF formation with increasing Al content in the MFI-Sn/Al  
501 catalysts suggests that the increased Brønsted acidity affected the performance of Lewis acidity  
502 from Sn sites, *i.e.*, promoted fructose formation from glucose isomerization and suppressed  
503 glucose conversion to side products and thus glucose conversion rate, which overall might be the  
504 consequences of cooperative catalysis between both types of acidity in a single catalyst for this  
505 three-step reaction cascade.

506 The comparison for glucose conversion and product yields between MFI-Sn/Al (100/50)  
507 and MFI-Sn/Al (50/50) catalysts in Fig. 9 and Fig. S2 (Section S1 in supplementary information)  
508 shows the effect of Sn sites (*i.e.*, Lewis acidity) on the performance of the hierarchical lamellar  
509 MFI-Sn/Al catalysts. The increase in Sn sites promoted the glucose conversion as well as HMF  
510 and EMF formation, while the fructose yield was reduced. It is suggested that Sn sites in zeolite

511 function as Lewis acidity that is beneficial for isomerization of glucose to fructose product,<sup>59</sup> and  
512 thus the higher glucose conversion and fructose formation are expected with increasing Sn sites  
513 while keeping Al site concentration in the MFI-Sn/Al catalysts. The discrepancy for observed  
514 lower fructose formation (or yield) and higher glucose conversion as well as higher HMF and  
515 EMF formation in this three-step reaction cascade hints that the cooperative catalysis between  
516 the Brønsted acidic Al–O(H)–Si sites and Lewis acidic Sn sites might exist for this observed  
517 catalytic results. The nearly complete conversion of glucose over each catalyst (Section S2 of the  
518 Supplementary Information) suggests that Sn sites in each MFI-Sn/Al catalyst are efficient for  
519 isomerization of glucose reactant in this reaction cascade. Overall, the increase in Sn or Al  
520 content in the catalyst facilitates the particular reaction step in the reaction cascade, which  
521 consequently influences the whole reaction network and exhibits different catalytic performances.  
522 A good balance between the two types of acid sites can be optimized to realize cooperative  
523 catalysis for further optimizing the EMF yield in glucose conversion in the reaction cascade. As  
524 shown in Fig. 9, the MFI-Sn/Al (50/50) zeolite showed best performance, with as high as ~44%  
525 EMF yield, among these four MFI-Sn/Al catalyst formulations.



526

527 **Fig. 9** Effect of Al and Sn contents in hierarchical lamellar MFI-Si/Al zeolites on conversion of  
 528 glucose to EMF at 413 K. (reaction condition: glucose: 0.090 g; zeolite: 0.074 g; time: 9 h;  
 529 ethanol: 3 mL).

### 530 Effect of carbohydrate type on EMF synthesis over MFI-Sn/Al (100/100) catalyst

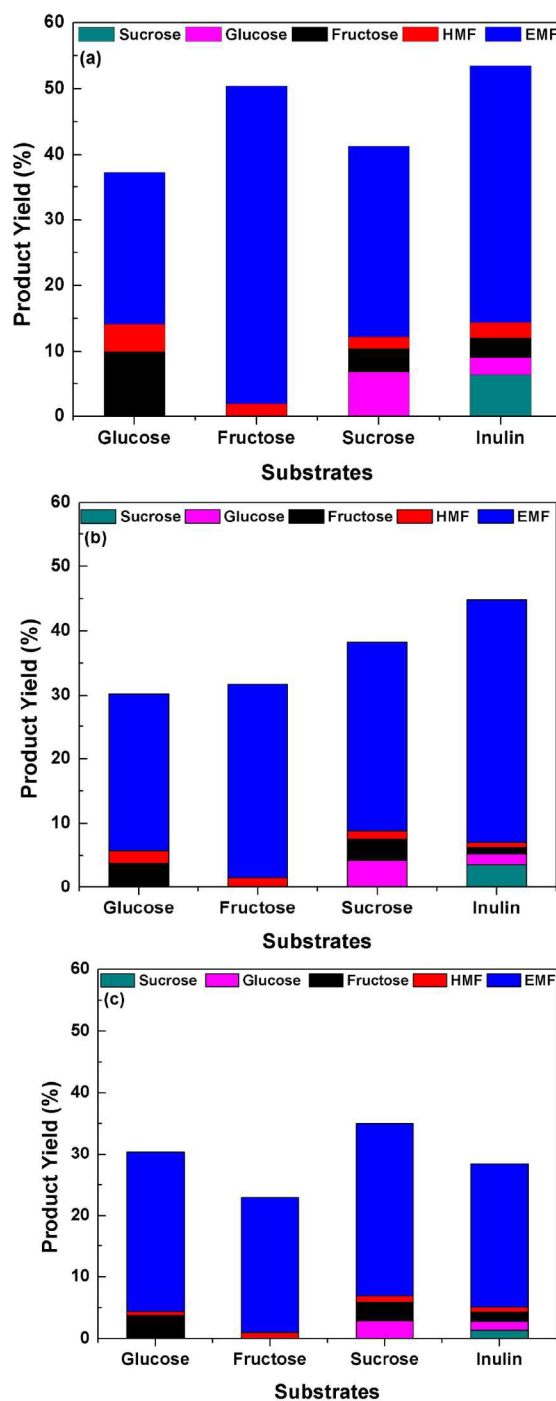
531 Glucose is one type of monosaccharides and simple carbohydrates in lignocellulosic biomass,  
 532 which has been shown the feasibility of conversion into EMF over the MFI-Sn/Al zeolite  
 533 catalysts. In reality, the natural biomass produces various types of saccharides, including other  
 534 monosaccharides, disaccharides and polysaccharides. To investigate the applicability of the  
 535 hierarchical lamellar MFI-Sn/Al in enabling reaction cascades for conversion of other types of  
 536 biomass feedstock into more valuable EMF product, we purposely studied the performance of  
 537 the MFI-Sn/Al (100/100) catalyst in EMF synthesis from fructose monosaccharide, sucrose  
 538 disaccharide and inulin polysaccharides (a polymer of ~24 fructose and 1 glucose units),  
 539 respectively. The effect of temperature on conversion of these carbohydrate feedstocks for EMF

540 production was also studied. For comparison purpose, the EMF yields from glucose conversion  
541 at different temperatures were included in this section.

542 Fig. 10 shows product yield from conversion of different carbohydrates over the MFI-Sn/Al  
543 (100/100) catalyst at the temperature of 398 K, 406 K, and 413 K, respectively. As shown in Fig.  
544 10a, the EMF yield at 398 K increases with the reactant changes from glucose, sucrose, inulin, to  
545 fructose in sequence. This trend is consistent with the fructose composition of the glucose,  
546 sucrose, inulin and fructose carbohydrates. It is known that glucose is a simple monosaccharide;  
547 Sucrose is a disaccharide that is composed of 1 glucose and 1 fructose units; Inulin is a  
548 polysaccharide that is comprised of 1 glucose and ~24 fructose units; and Fructose is a simple  
549 monosaccharide. The formation of EMF from fructose only needs to go through a two-step  
550 (dehydration of fructose to HMF and etherification of HMF to EMF) reaction cascade, which  
551 eases the reaction network. The increase in fructose units in these four reactants incrementally  
552 shifts the reaction cascade from three steps to two steps, and thus leads to higher EMF yield. It  
553 should be noted that reaction intermediates were all observed in these reaction cascades over the  
554 MFI-Sn/Al (100/100) catalyst, although EMF is the major product. For example, when sucrose  
555 was used as the reactant, the glucose, fructose and HMF reaction intermediates in minor  
556 quantities were all observed. This indicates the occurrence of the reaction cascade effectively  
557 enabled by the dual Lewis and Brønsted acidic catalyst. The nearly complete conversion of each  
558 carbohydrate reactant and fast reactant conversion rates (see Figs. S3-S5 in section S3 of the  
559 Supplementary Information) indicates that mass transport limitation is negligible due to the dual  
560 meso-/microporosity in the hierarchical lamellar MFI-Sn/Al (100/100) catalyst.

561 Figs. 10b and c show the product yields from carbohydrate conversion over the MFI-Sn/Al  
562 (100/100) catalyst at 406 K and 413 K, respectively. First of all, EMF is still the major product

563 although the total detectable product yields are decreased at different degrees with respect to  
564 different reactant with increasing reaction temperature. Specifically, the EMF yield from glucose  
565 reactant slightly increases with the reaction temperature, as discussed above. The EMF yield  
566 keeps almost constant from the sucrose reactant, while it decreases significantly with the  
567 increasing temperature from the fructose and inulin carbohydrate reactants. The changes in EMF  
568 yield from different reactants over the MFI-Sn/Al catalyst reveal that higher temperature benefits  
569 isomerization of glucose than dehydration of fructose and etherification of HMF to EMF product.  
570 The decrease in the EMF yield from fructose and inulin may be caused by the increased side  
571 reactions along with the reaction cascade with increasing reaction temperature.



572

573 **Fig. 10** Effect of carbohydrate reactants on synthesis of EMF over MFI-Sn/Al (100/100) at  
574 temperature of (a) 398 K, (b) 406 K, and (c) 413 K, respectively. (reaction condition:  
575 carbohydrate reactant: 0.090 g; zeolite: 0.074 g; time: 9 h; ethanol: 3 mL)

## 576 **Conclusions**

577 The hierarchical lamellar MFI-Sn/Al zeolites that comprise of dual meso-/microporosity and  
578 dual Lewis acidic Sn and Brønsted acidic Al–O(H)–Si sites in single zeolite particles have been  
579 successfully prepared. The one-step crystallization of MFI zeolites in the presence of both Sn  
580 and Al precursors under the assistance of the diquatery ammonium template has been simply  
581 employed to create this multifunctional MFI-Sn/Al zeolite. The morphology and textural  
582 property measurements confirm the presence of mesoporosities in these zeolite catalysts. The  
583 acidity characterizations show the existence of dual types of acidity and variations of these  
584 acidities with the Si/Al and Si/Sn ratios in the zeolite synthesis recipe. As a consequence of the  
585 dual porosity and acidity features, the MFI-Sn/Al zeolites were studied as catalysts for  
586 conversion of glucose into EMF product in ethanol solvent. The reaction proceeded via the  
587 isomerization of glucose to fructose over Lewis acidic Sn-sites and dehydration of fructose to  
588 HMF and then etherification of HMF and ethanol to EMF over the Brønsted acidic Al–O(H)–Si  
589 sites. The dual meso-/microporosity in the MFI-Sn/Al zeolites facilitated mass transport in  
590 processing of bulky molecules involved in this reaction cascade. The balance between two types  
591 of acidities possibly facilitated the cooperative catalysis, which led to as high as 44% from the  
592 glucose reactant. The co-existence of multiple acidities and porosities in one single zeolite  
593 catalyst enabled one-pot cascade reactions for carbohydrate upgrading, which is potentially  
594 applicable for processing of other complex reaction network for efficient production of end  
595 chemicals/fuels from renewable biomass resources.

## 596 **Acknowledgements**

597 The authors gratefully acknowledge the support from the National Science Foundation (NSF-  
598 CBET 1642405, 1705284 and 1351384). This work is supported in part by the U. S. Army

599 Research Laboratory (contract/grant number: W911NF-16-2-0036) and the U. S. Army Research  
600 Office (contract/grant number: W911NF-17-1-0363). The authors also acknowledge the support  
601 of the Maryland NanoCenter and its NispLab. The NispLab is supported in part by the NSF as a  
602 MRSEC Shared Experimental Facility. Y. Bai acknowledges China National Science Foundation  
603 (No. 31470605) for financial support for her study at University of Maryland.

604  
605  
606 **Supplementary information available:** Morphology and textural properties of MFI-Sn/Al  
607 zeolites; the glucose conversion and product yields versus reaction time over the MFI-Sn/Al  
608 zeolite with variable Si/Sn and Si/Al ratios; and the EMF synthesis versus reaction time from  
609 different carbohydrate reactants at different reaction temperatures over the MFI-Sn/Al (100/100)  
610 zeolite catalyst.

611  
612  
613  
614  
615  
616  
617  
618  
619  
620  
621

622 **References**

- 623 1 A. Brandt, J. Gräsvik, J. P. Hallett and T. Welton, *Green Chem.*, 2013, **15**, 550-583.
- 624 2 A. J. Ragauskas, C. K. Williams, B. H. Davison, G. Britovsek, J. Cairney, C. A. Eckert, W.  
625 J. Frederick, J. P. Hallett, D. J. Leak and C. L. Liotta, *Science*, 2006, **311**, 484-489.
- 626 3 R. Xing, A. V. Subrahmanyam, H. Olcay, W. Qi, G. P. van Walsum, H. Pendse and G. W.  
627 Huber, *Green Chem.*, 2010, **12**, 1933-1946.
- 628 4 A. Demirbaş, *Energy Convers. Manage.*, 2001, **42**, 1357-1378.
- 629 5 A. Liu, Z. Zhang, Z. Fang, B. Liu and K. Huang, *J. Ind. Eng. Chem.*, 2014, **20**, 1977-1984.
- 630 6 J. B. Binder and R. T. Raines, *J. Am. Chem. Soc.*, 2009, **131**, 1979-1985.
- 631 7 J. N. Chheda, G. W. Huber and J. A. Dumesic, *Angew. Chem. Int. Ed.*, 2007, **46**, 7164-7183.
- 632 8 Y. Zhang, Z. Xue, J. Wang, X. Zhao, Y. Deng, W. Zhao and T. Mu, *RSC Adv.*, 2016, **6**,  
633 51229–51237.
- 634 9 M. Balakrishnan, E. R. Sacia and A. T. Bell, *Green Chem.*, 2012, **14**, 1626-1634.
- 635 10 E. Taarning, I. S. Nielsen, K. Egeblad, R. Madsen and C. H. Christensen, *ChemSusChem*,  
636 2008, **1**, 75-78.
- 637 11 P. Che, F. Lu, J. Zhang, Y. Huang, X. Nie, J. Gao and J. Xu, *Bioresour. Technol.*, 2012, **119**,  
638 433-436.
- 639 12 C. M. Lew, N. Rajabbeigi and M. Tsapatsis, *Ind. Eng. Chem. Res.*, 2012, **51**, 5364-5366.
- 640 13 H. Wang, T. Deng, Y. Wang, Y. Qi, X. Hou and Y. Zhu, *Bioresour. Technol.*, 2013, **136**,  
641 394-400.
- 642 14 B. Liu, Z. Zhang and K. Huang, *Cellulose*, 2013, **20**, 2081-2089.
- 643 15 H. Wang, T. Deng, Y. Wang, X. Cui, Y. Qi, X. Mu, X. Hou and Y. Zhu, *Green Chem.*,  
644 2013, **15**, 2379-2383.

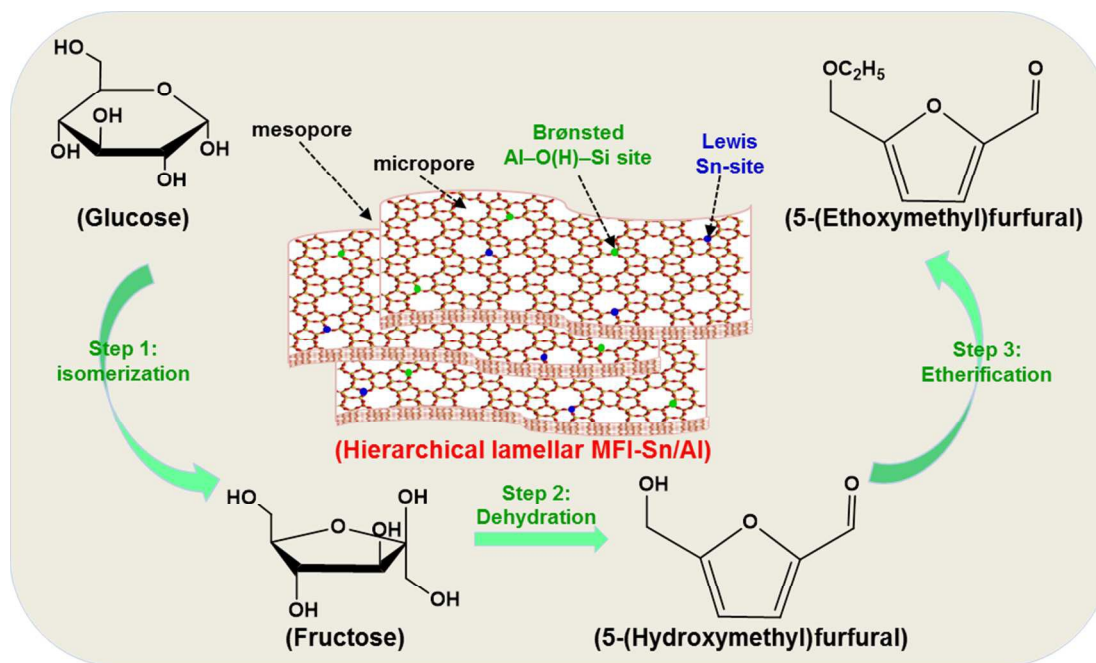
- 645 16 Y. Yang, M. M. Abu-Omar and C. Hu, *Appl. Energy*, 2012, **99**, 80-84.
- 646 17 Z. Zhang, Y. Wang, Z. Fang and B. Liu, *ChemPlusChem*, 2013, **79**, 233-240.
- 647 18 R. Bermejo-Deval, R. S. Assary, E. Nikolla, M. Moliner, Y. Román-Leshkov, S. Hwang, A.  
648 Palsdottir, D. Silverman, R. F. Lobo, L. A. Curtiss and M. E. Davis, *Proc. Nati. Acad. Sci.*,  
649 2012, **109**, 9727-9732.
- 650 19 E. Nikolla, Y. Román-Leshkov, M. Moliner and M. E. Davis, *ACS Catal.*, 2011, **1**, 408-410.
- 651 20 Y. Román-Leshkov, M. Moliner, J. A. Labinger and M. E. Davis, *Angew. Chem. Int. Ed.*,  
652 2010, **49**, 8954-8957.
- 653 21 M. Choi, K. Na, J. Kim, Y. Sakamoto, O. Terasaki and R. Ryoo, *Nature*, 2009, **461**, 246-  
654 249.
- 655 22 D. Liu, A. Bhan, M. Tsapatsis and S. A. Hashimi, *ACS Catal.*, 2011, **1**, 7-17.
- 656 23 L. Emdadi, Y. Wu, G. Zhu, C. C. Chang, W. Fan, T. Pham, R. F. Lobo and D. Liu, *Chem.*  
657 *Mater.*, 2014, **26**, 1345-1355.
- 658 24 N. K. Mal, V. Ramaswamy, P. R. Rajamohanam and A. V. Ramaswamy, *Microporous*  
659 *Mater.*, 1997, **12**, 331-340.
- 660 25 W. E. Farneth and R. J. Gorte, *Chem. Rev.*, 1995, **95**, 615-635.
- 661 26 O. A. Abdelrahman, K. P. Vinter, L. Ren, D. Xu, R. J. Gorte, M. Tsapatsis and P. J.  
662 Dauenhauer, *Catal. Sci. Technol.*, 2017, **7**, 3831-3841.
- 663 27 W. Kim, X. Zhang, J. S. Lee, M. Tsapatsis and S. Nair, *ACS nano*, 2012, **6**, 9978-9988.
- 664 28 S. F. Zhao, X. T. Yao, B. H. Yan, L. Li, Y. M. Liu and M. Y. He, *Chin. Chem. Lett.*, 2017,  
665 **28**, 1318-1323.

- 666 29 A. G. Machoke, I. Y. Knoke, S. Lopez-Orozco, M. Schmiele, V. R. R. Marthala, E. Spiecker,  
667 T. Unruh, M. Hartmann and W. Schwieger, *Microporous Mesoporous Mater.*, 2014, **190**,  
668 324-333.
- 669 30 W. Park, D. Yu, K. Na, K. E. Jelfs, B. Slater, Y. Sakamoto and R. Ryoo, *Chem. Mater.*,  
670 2011, **23**, 5131-5137.
- 671 31 K. S. W. Sing, D. H. Everett, R. A. W. Haul, L. Moscou, R. A. Rouquerol and T.  
672 Siemieniewska, *Pure Appl. Chem.*, 1985, **57**, 603-619.
- 673 32 M. Thommes, Elsevier Science & Technology, 2007; pp 495–525.
- 674 33 R. Aiello, F. Crea, F. Testa, G. Demortier, P. Lentz, M. Wiame and J. B. Nagy,  
675 *Microporous Mesoporous Mater.*, 2000, **35**, 585-595.
- 676 34 S. L. Burkett and M. E. Davis, *J. Phys. Chem.*, 1994, **98**, 4647-4653.
- 677 35 M. A. Camblor, A. Corma, M. J. Díaz-Cabañas and C. Baerlocher, *J. Phys. Chem. B*, 1998,  
678 **102**, 44-51.
- 679 36 W. Kolodziejski, C. Zicovich-Wilson, C. Corell, J. Pérez-Pariente and A. Corma, *J. Phys.*  
680 *Chem.*, 1995, **99**, 7002-7008.
- 681 37 S. Maheshwari, C. Martínez, M. T. Portilla, F. J. Llopis, A. Corma and M. Tsapatsis, *J.*  
682 *Catal.*, 2010, **272**, 298-308.
- 683 38 D. Liu, A. Bhan, M. Tsapatsis and S. A. Hashimi, *ACS Catal.*, 2011, **1**, 7-17.
- 684 39 D. Coster, A. L. Blumenfeld and J. J. Fripiat, *J. Phys. Chem.*, 1994, **98**, 6201-6211.
- 685 40 J. P. Gilson, G. C. Edwards, A. W. Peters, K. Rajagopalan, R. F. Wormsbecher, T. G.  
686 Roberie and M. P. Shatlock, *J. Chem. Soc., Chem. Commun.*, 1987, **0**, 91-92.
- 687 41 P. Y. Dapsens, C. Mondelli, J. Jagielski, R. Hauert and J. Pérez-Ramírez, *Catal. Sci.*  
688 *Technol.*, 2014, **4**, 2302-2311.

- 689 42 G. Busca, *Catal. Today*, 1998, **41**, 191-206.
- 690 43 M. Trombetta and G. Busca, *J. Catal.*, 1999, **187**, 521-523.
- 691 44 M. Jiang and H.G. Karge, *J. Chem. Soc., Faraday Trans.*, 1996, **92**, 2641-2649.
- 692 45 S. Schallmoser, T. Ikuno, M. F. Wagenhofer, R. Kolvenbach, G. L. Haller, M. Sanchez-  
693 Sanchez and J. A. Lercher, *J. Catal.*, 2014, **316**, 93-102.
- 694 46 W. N. P. van der Graaff, C. H. L. Tempelman, E. A. Pidko and E. J. M. Hensen, *Catal. Sci.*  
695 *Technol.*, 2017, **7**, 3151–3162.
- 696 47 P. Bräuer, P. L. Ng, O. Situmorang, I. Hitchcock and C. D’Agostino, *RSC Adv.*, 2017, **7**,  
697 52604–52613.
- 698 48 A. Platon and W. J. Thomson, *Ind. Eng. Chem. Res.*, 2003, **42**, 5988-5992.
- 699 49 S. Roy, K. Bakhmutsky, E. Mahmoud, R. F. Lobo and R. J. Gorte, *ACS Catal.*, 2013, **3**, 573-  
700 580.
- 701 50 M. Boronat, P. Concepción, A. Corma, M. Renz and S. Valencia, *J. Catal.*, 2005, **234**, 111-  
702 118.
- 703 51 L. Ren, Q. Guo, P. Kumar, M. Orazov, D. Xu, S. M. Alhassan, K. A. Mkhoyan, M. E. Davis  
704 and M. Tsapatsis, *Angew. Chem. Int. Ed.*, 2015, **54**, 10848-10857.
- 705 52 H. Liu, Y. Li, W. Shen, X. Bao and Y. Xu, *Catal. Today*, 2004, **93**, 65-73.
- 706 53 D. Ma, W. Zhang, Y. Shu, X. Liu, Y. Xu and X. Bao, *Catal. Lett.*, 2000, **66**, 155-160.
- 707 54 Q. Zhao, W. H. Chen, S. J. Huang, Y. C. Huang, H. K. Lee and S. B. Liu, *J. Phys. Chem. B*,  
708 2002, **106**, 4462-4469.
- 709 55 W. E. Fameth, *Chem. Rev.*, 1995, **95**, 615-635.
- 710 56 M. Niwa and N. Katada, *Chem. Rec.*, 2013, **13**, 432-455.
- 711 57 N. Katada, H. Igi, J. H. Kim and M. Niwa, *J. Phys. Chem. B*, 1997, **101**, 5969-5977.

- 712 58 E. Sjöman, M. Mänttari, M. Nyström, H. Koivikko and H. Heikkilä, *J. Membr. Sci.*, 2007,  
713 **292**, 106-115.
- 714 59 Y. Román-Leshkov, M. Moliner, J. A. Labinger and M. E. Davis, *Angew. Chem. Int. Ed.*,  
715 2010, **49**, 8954-8957.

## Table of contents:



Glucose conversion over hierarchical lamellar MFI-Sn/Al: accommodating three-step reaction cascade over one single catalyst for high yield production of 5-(ethoxymethyl)furfural.